Materials Science & Engineering R 171 (2026) 101283

Contents lists available at ScienceDirect

Materials Science & Engineering R

journal homepage: www.elsevier.com/locate/mser

Cooperative thermal crystallization enables interfacial homogenization in antisolvent- and HTL-free Sn-Pb perovskite solar cells

Yun-Shan Li [a,1], Wen-Xian Zhu [a,1], Xin Chen [b], Yueyao Dong [c], Huan-Wei Lin [d], Yi-Sheng Lin [a], Yun-Sheng Shih [e], Chi-Jing Huang [a], Wei-Jia Qiu [d], Chang-Hao Wang [a], Chih-Chan Tsai [c], Luis Lanzetta [g], Matyas Daboczi [i], Caterina Ducati [b], Eric Wei-Guang Diau [e,f,*], Thomas J. Macdonald [c,*], Chieh-Ting Lin [a,d,h,*]

[a] Department of Chemical Engineering, National Chung Hsing University, Taichung, 40227, Taiwan
[b] Department of Materials Science and Metallurgy, University of Cambridge, Cambridge, CB3 0FS, UK
[c] Department of Electronic & Electrical Engineering, University College London, London, WC1E 7JE, UK
[d] Graduate Program in Semiconductor and Green Technology, Academy of Circular Economy, National Chung Hsing University, Nantou County 540, Taiwan
[e] Department of Applied Chemistry and Institute of Molecular Science, National Yang Ming Chiao Tung University, 1001 Ta-Hseuh Rd., Hsinchu, 300093, Taiwan
[f] Center for Emergent Functional Matter Science, National Yang Ming Chiao Tung University, 1001 University Road, Hsinchu, 30010, Taiwan
[g] Institute of Advanced Materials (INAM), Jaume I University, Av. de Vicent Sos Baynat S/N, Castelló de la Plana, 12006, Spain
[h] Innovation and Development Center of Sustainable Agriculture, National Chung Hsing University, Taichung, 40227, Taiwan
[i] HUN-REN Centre for Energy Research, Institute of Technical Physics and Materials Science, Budapest, 1121, Hungary

ARTICLE INFO

Keywords:
Sn–Pb Perovskites
Perovskite solar cells
Cooperative Crystallization
Interfacial Homogenization
HTL-Free Solar Cells

ABSTRACT

Low-bandgap Sn-Pb perovskite solar cells are indispensable building blocks for all-perovskite tandems, yet their development is constrained by challenging crystallization control, severe interfacial recombination, and reliance on costly hole transport layers (HTLs) and antisolvent processing involving hazardous and volatile organic solvents. Here, a GuaSCN-assisted vacuum crystallization strategy is developed to realize efficient HTL-free and antisolvent-free Sn-Pb perovskite solar cells. The in-situ photoluminescence evolution is consistent with a cooperative crystallization process, where SCN^- regulates early-stage growth while Gua^+ facilitates later-stage structural relaxation, enabling sustained optoelectronic improvement during film formation. This synergistic regulation yields compact Sn-Pb perovskite films with a uniform buried interface, reduced structural and compositional heterogeneity, and a surface-associated residual region that may contribute to interfacial passivation. Cross-sectional chemical mapping further shows reduced local compositional fluctuations and interfacial irregularity within the analysed regions. These structural characteristics are accompanied by increased quasi-Fermi level splitting, reduced energetic disorder, and a higher attainable photovoltage of the neat perovskite film. Consequently, HTL-free devices deliver a champion efficiency of 21.4% with a fill factor exceeding 80%, among the highest values reported for HTL-free, antisolvent-free Sn-Pb perovskite solar cells. Furthermore, the GuaSCN-treated narrow-bandgap subcell is integrated into a monolithic all-perovskite tandem device, demonstrating its promise for simplified tandem photovoltaics.

1. Introduction

Perovskite materials have revolutionised the field of photovoltaics, offering a promising pathway to high-efficiency and cost-effective solar cells. [1] Among these materials, mixed tin-lead (Sn-Pb) perovskites have emerged as a compelling alternative to traditional lead-based perovskites.[2–4] The partial substitution of lead (Pb) with tin (Sn) addresses environmental and health concerns and allows for tuneable bandgap properties. In particular, Sn-Pb perovskites have shown great potential for use in all-perovskite tandem solar cells, where their near-infrared light absorption enables efficient solar spectrum utilisation.[5–8] Despite recent advancements, the development of Sn-Pb

* Corresponding author at: Department of Chemical Engineering, National Chung Hsing University, Taichung 40227, Taiwan.
E-mail addresses: diau@nycu.edu.tw (E.W.-G. Diau), tom.macdonald@ucl.ac.uk (T.J. Macdonald), c.lin15@nchu.edu.tw (C.-T. Lin).
[1] The authors contributed equally to this work.

https://doi.org/10.1016/j.mser.2026.101283
Received 8 June 2026; Received in revised form 8 August 2026; Accepted 20 August 2026
Available online 31 August 2026

perovskite solar cells (PSCs) still faces significant challenges. These include the instability of the perovskite layer caused by Sn^{2+} oxidation, [9,10] the inhomogeneous Sn and Pb distribution resulting from differing crystallization kinetics in mixed Sn-Pb perovskite films [11, 12], and power conversion efficiency (PCE) losses at the interface between the perovskite and the transport layers. [2–4,13–15]

In inverted p-i-n Sn-Pb perovskite solar cells, the hole transport layer (HTL) is a key functional layer within the device architecture. It should offer well-matched energy levels to promote efficient hole collection while remaining chemically and electronically stable so as not to compromise device durability. Furthermore, the HTL surface can strongly influence the nucleation and crystallization of the Sn-Pb perovskite film formed above it, thereby affecting the resulting film quality and device performance. [16] One of the most widely used HTLs for Sn-Pb PSCs is poly(3,4-ethylenedioxythiophene): polystyrenesulfonate (PEDOT:PSS). However, the acidic and hygroscopic nature of PEDOT:PSS can accelerate degradation processes and facilitate ion migration, while its highly doped state often leads to pronounced interfacial recombination losses. [17,18] As such, many approaches have been shown to modify PEDOT:PSS, such as hydroquinone [3], polyethylene glycol [19] and sodium hydroxide [17]. In addition to these modifications, other HTLs have also been proposed to replace PEDOT:PSS, such as polymeric HTLs, [4,20] NiOx [21]and hole selective self-assembled monolayers (SAMs). [2] However, these layers might introduce other challenges, including increased fabrication complexity, higher costs, and potential instability due to their susceptibility to environmental factors such as moisture and oxygen. [22]

One promising approach to overcoming these challenges involves the use of HTL-free structures in inverted perovskite solar cells (PSCs). This strategy has gained attention due to its potential to simplify device fabrication and enhance stability. However, exploring HTL-free designs in low-bandgap PSCs has been limited, with only a few studies addressing this configuration. [22–24] Several studies have introduced additional interfacial layers to modify the surface properties of transparent conductive oxides (TCOs). [23,24] For example, Ma *et al.* propose that coating indium tin oxide (ITO) electrodes with a layer of taurine, a Brønsted-Lowry acid without charge-selective properties, helps align the energy levels with the Sn-Pb perovskite film, resulting in enhanced stability and improved PCE. [24] Another approach is to modify the perovskite layer via additive engineering. [25,26] Kim *et al.* improved hole transfer in Sn-Pb perovskite solar cells without using a standalone hole transport layer by introducing CuSCN and glycine hydrochloride (GlyHCl) as perovskite precursor solution additives. Although CuSCN is commonly used as an HTL material, here it acts as an additive within the perovskite layer, enhancing hole mobility and improving band alignment with ITO to boost device performance. [26] Moreover, the selection of a transparent electrode is crucial for HTL-free device structures. Hydrogen-doped indium oxide surpasses conventional TCOs like ITO and fluorine-doped tin oxide (FTO) in HTL-free Sn-Pb PSCs by reducing parasitic absorption losses in the near-infrared region and promoting better perovskite nucleation due to its smoother surface. [27] However, HTL-free Sn-Pb perovskite devices often exhibit reduced fill factors and low shunt resistance. [25,26,28–32] In addition, the direct growth of perovskite films on bare electrodes can result in imperfect interfacial coverage, where local voids or morphological inhomogeneities may further facilitate non-ideal charge transport and shunting losses. [22]

Another critical aspect of improving Sn-Pb PSCs is the development of antisolvent-free processing techniques. Traditional perovskite fabrication methods often use antisolvents during crystallization to achieve high-quality perovskite films. [33] While effective, conventional antisolvent processing may involve hazardous and volatile solvents, along with additional processing complexity and variability in film quality. [34] Antisolvent-free processing techniques require optimising the composition of precursor solution and the parameters of deposition to form high-quality perovskite films without antisolvents. This approach offers several benefits, including environmental friendliness, simplified fabrication, and improved film uniformity. Initial efforts in antisolvent-free Sn-Pb perovskite fabrication have focused primarily on devices with HTLs. [35–38] In contrast, HTL-free Sn-Pb perovskite solar cells made through antisolvent-free approaches remain largely unexplored. In such systems, controlling crystallization without the aid of antisolvents becomes particularly important due to the need of growing homogenous films and high-quality interfaces with adjacent TCOs. Additive engineering has therefore emerged as an effective strategy to regulate crystallization kinetics and improve film morphology. Among these additives, guanidinium thiocyanate (GuaSCN) is particularly well established. The seminal work of Tong *et al.* demonstrated that GuaSCN markedly improves the structural and optoelectronic properties of low-bandgap Sn-Pb perovskites, [39] and our recent study further revealed its role in modulating the crystal-growth pathway of antisolvent-processed Sn-Pb films. [40] However, both studies employed HTL-coated substrates and antisolvent-assisted crystallization. Whether these benefits persist when the perovskite crystallizes directly on bare ITO under vacuum-assisted processing, and how GuaSCN directs film formation in this configuration, remain unresolved.

In this work, we employ in-situ photoluminescence (PL) measurements to monitor the optoelectronic evolution of Sn-Pb perovskite films during the annealing stage following vacuum-assisted crystallization quenching (VACQ) in an HTL-free architecture. Rather than revisiting the established beneficial effects of GuaSCN, this study focuses on the direct connection between GuaSCN-assisted VACQ processing, buried-interface formation on bare ITO, and the associated device losses. The GuaSCN-containing formulation exhibits a distinctive two-stage PL evolution during the post-VACQ thermal treatment, consistent with complementary contributions arising from the simultaneous presence of Gua^+ and SCN^-. Correlative structural, interfacial, and optoelectronic characterization further indicates that GuaSCN-assisted VACQ promotes compact film formation with improved buried-interface continuity and reduced local structural and energetic heterogeneity, thereby mitigating non-radiative recombination losses. Consequently, the HTL-free devices achieve power conversion efficiencies exceeding 21% with fill factors above 80%.

2. Result and discussion

To investigate the evolution of the optoelectronic properties of Sn-Pb perovskites during thermal annealing after the VACQ process, an in-situ photoluminescence (PL) monitoring setup was integrated into the film fabrication process, as illustrated in Fig. 1**a**. In this protocol, the perovskite films underwent a VACQ treatment after spin-coating, followed by flash annealing at 100 °C for 10 min on the first hot plate, followed by immediate transfer to a second hot plate maintained at 65 °C for an additional 10 min of mild thermal relaxation. For clarity, the in-situ PL data are presented only for the first 10 s at 100 °C and the first 300 s at 65 °C, as the PL intensity remained nearly unchanged afterward. This annealing procedure was performed to avoid glovebox vapor ingress for the as prepared films. [41] A detailed description of sample preparation is provided in the Supplementary Information (Experimental Section).

To further investigate the formulation-dependent effects associated with GuaSCN in this crystallization process, we systematically compared three additives, namely GuaI as the Gua^+ source, $Pb(SCN)_2$ as the SCN^- source, and GuaSCN containing both components, and a control sample without any of these additives. Although these formulations do not provide a chemically isolated comparison of Gua^+ and SCN^-, they enable formulation-dependent trends associated with the corresponding precursor chemistries to be examined while avoiding the introduction of counterions entirely foreign to the parent Sn-Pb precursor system. [42] The thermal PL evolution associated with the VACQ treatment were further investigated by in-situ PL measurements performed during the thermal annealing steps. As shown in Fig. 1**b**, the PL contour plots were recorded during the thermal treatment, and the temporal evolution of

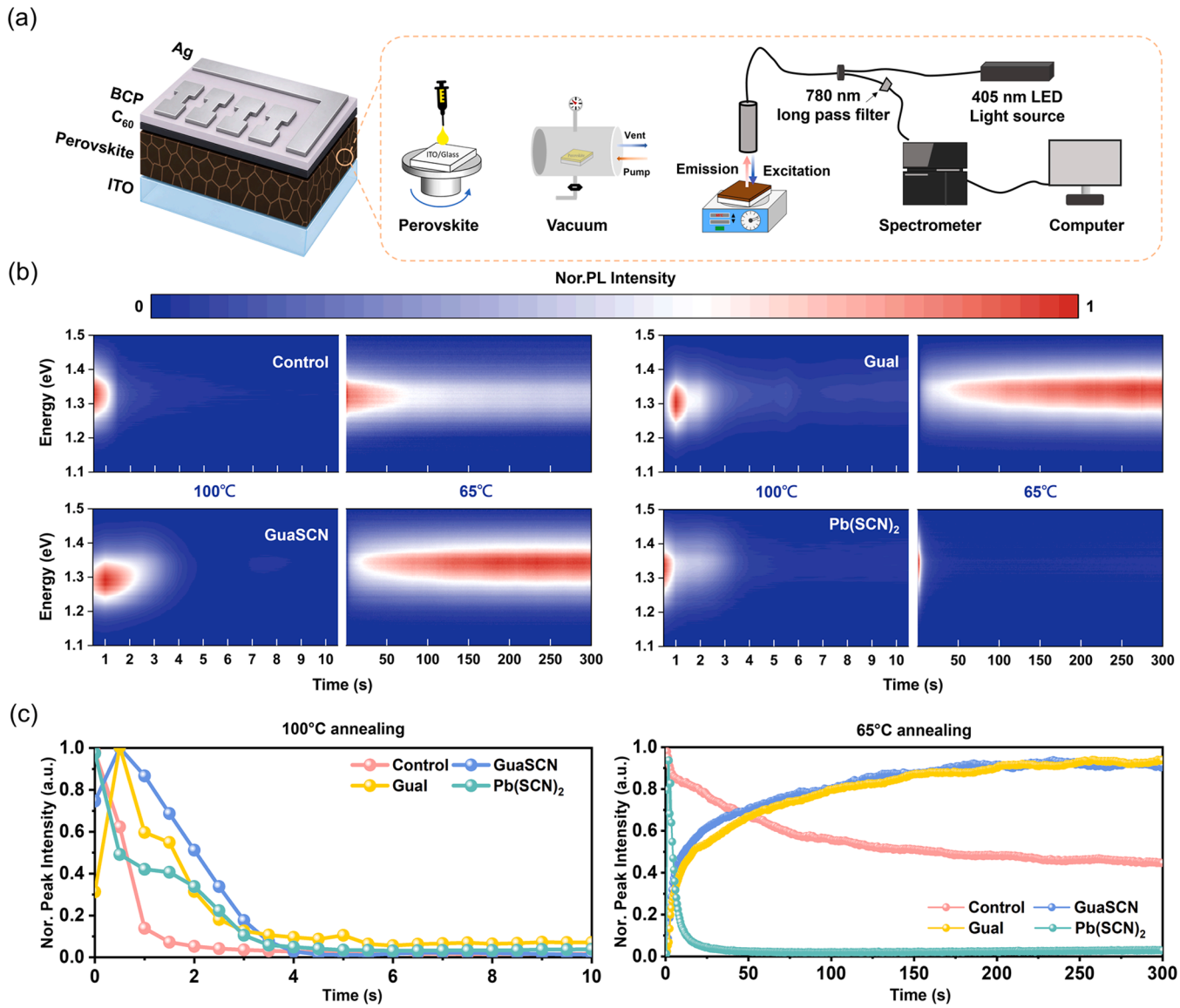

Fig. 1. (a) Schematic illustration of the HTL-free device structure and the in-situ PL setup used to monitor the VACQ process. (b) Time-resolved in-situ PL contour plots of the control, GuaI-, GuaSCN-, and $Pb(SCN)_2$-treated films during the 100 °C annealing stage (left panels) and the subsequent 65 °C stage (right panels). (c) Corresponding temporal evolution of the normalized PL peak intensity during the 100 °C annealing stage (left) and the 65 °C stage (right).

the PL peak intensity is summarized in Fig. 1**c**, where each PL trace was independently normalized to its own maximum intensity. The PL peak-energy evolution, linewidth (FWHM) evolution, and replicate measurements are shown in Figure S1 **and** Figure S2.

Clear differences first emerge during the 100 °C annealing stage. The control film undergoes rapid PL quenching, indicating that substantial non-radiative recombination develops quickly during thermal processing. $Pb(SCN)_2$ also shows pronounced PL decay, but with a discernible trailing response relative to the reference, suggesting that SCN^- influences the crystallization behaviour during thermal annealing rather than being completely inactive under these conditions. However, this effect alone is insufficient to preserve high optoelectronic quality. In comparison, both GuaI- and GuaSCN-treated films retain markedly higher PL intensity throughout this stage, suggesting that Gua^+ is associated with a more favourable optoelectronic evolution during thermal annealing. Notably, GuaSCN exhibits the slowest PL quenching, requiring 5 s to approach the strongly quenched state compared with 2 s for the control, suggesting that the combined presence of Gua^+ and SCN^- most effectively delays the build-up of non-radiative loss during annealing and promotes a more gradually evolving crystallization pathway.

More pronounced differences are observed during the subsequent 65 °C stage. Both GuaI and GuaSCN display pronounced PL recovery, suggesting that Gua-containing precursor chemistry is associated with the later-stage optoelectronic recovery during thermal annealing. This behaviour is consistent with our previous study, which demonstrated strong PL recovery in antisolvent-processed Sn-Pb films of nearly identical composition deposited on an HTL. [40] Notably, the same additive-dependent response is observed here for films crystallized directly on bare ITO under VACQ processing, indicating that this behaviour is not specific to antisolvent-assisted crystallization or HTL-coated substrates. Building on the beneficial effects of GuaSCN established in these systems, [39,40] the focus of the present work is therefore on how this response relates to buried-interface formation and the associated device losses in the HTL-free architecture, as examined below. In contrast, the control film shows only limited recovery, while $Pb(SCN)_2$ remains strongly quenched, confirming that SCN^- alone does not induce this later-stage relaxation behaviour.

Importantly, although GuaI and GuaSCN exhibit similarly strong PL recovery during the 65 °C stage, their final film properties differ

substantially. The final annealed GuaSCN-treated film shows the strongest steady-state PL intensity among the investigated samples, indicating suppressed non-radiative recombination (Figure S3). Top-view scanning electron microscopy (SEM) images further reveal a more compact and continuous surface morphology for the GuaSCN-treated film, while the $Pb(SCN)_2$- and GuaI-treated films show only partial improvement (Figure S4). XRD patterns confirm that all films retain the characteristic Sn-Pb perovskite diffraction features after annealing, suggesting that GuaSCN improves film formation without substantially altering the primary perovskite framework (Figure S5). Together, these observations are consistent with complementary effects arising from the combined GuaSCN precursor chemistry, which correlate with improved final film quality.

On the basis of the distinct PL evolution observed in Fig. 1, the control and GuaSCN-treated films were selected for detailed structural comparison in the following discussion. Grazing-incidence wide-angle X-ray scattering (GIWAXS) measurements were then performed to examine their final structural characteristics after annealing (Fig. 2**a-f**). Both films show the characteristic diffraction features of the 3D Sn-Pb perovskite phase, confirming the formation of the perovskite framework after annealing. However, clear differences are observed in the detailed scattering patterns. Compared with the control film, the GuaSCN-treated sample exhibits more segmented and spotty diffraction rings for the major perovskite reflections, indicating a more azimuthally anisotropic intensity distribution. [43] To quantitatively evaluate the crystallographic orientation distribution, azimuthal intensity profiles were extracted from the major 3D perovskite diffraction ring at incidence angles of 0.1° and 0.5° (Figure S6 **and** Table S1). The dominant azimuthal peaks are centered near $\chi = 90°$, consistent with a preferential out-of-plane orientation of the corresponding perovskite planes. At an incidence angle of 0.1°, the azimuthal FWHM decreases from approximately 9.3° for the control film to 4.0° for the GuaSCN-treated film. A similar reduction from approximately 8.1° to 4.3° is observed at 0.5°. These narrower azimuthal intensity distributions are consistent with a more concentrated out-of-plane crystallographic orientation distribution after GuaSCN treatment under both measurement conditions. [44] Nevertheless, the segmented character of the diffraction rings may also be influenced by discrete coherent scattering domains; therefore, the azimuthal analysis is used to quantify the dominant orientation distribution rather than to independently determine domain size. The measurements performed at different incidence angles provide structural information with different relative depth sensitivities. Incidence angles of 0.03°–0.10° are considered predominantly surface-weighted, whereas 0.20° provides greater contributions from the intermediate and deeper regions of the film. At an incidence angle of 0.50°, the detectable ITO-related scattering indicates that the measurement includes contributions from the full perovskite film thickness and the buried interface. Accordingly, the incidence-angle-dependent measurements are interpreted only in terms of relative depth sensitivity rather than layer-specific structural information.

In addition to the 3D perovskite reflections, weak low-q features assignable to 2D-related structural motifs are observed in both samples, while the GuaSCN-treated film also shows a detectable PbI_2-related diffraction signal. The fitted peak positions, corresponding d-spacings, and FWHM values of the 2D- and PbI_2-related features are summarized in Table S2. Compared with the control film, the low-q diffraction feature of the GuaSCN-treated film shifts toward higher q, corresponding to a smaller apparent d-spacing. The 2D-related feature is likely associated with the glycine-containing precursor formulation used in both films, consistent with previous reports that glycine-based additives can promote low-dimensional perovskite motifs in Sn-Pb systems. [45–47] Although this diffraction feature is assigned as 2D-perovskite-related, its exact chemical composition and crystallographic identity cannot be uniquely determined from the present GIWAXS data.

Notably, in the GuaSCN-treated film, the 2D-related and PbI_2-related features exhibit a directional distribution similar to that of the main 3D perovskite reflections, whereas the corresponding 2D-related signal in the control film appears more diffuse and less directionally defined. These results are consistent with GuaSCN mainly improving the structural coherence and spatial organization of residual 2D-/PbI_2-related features, rather than simply introducing new secondary phases. Such directionally correlated residual phases may contribute to interfacial passivation when present in limited amounts. [48,49]

Cross-sectional scanning transmission electron microscopy (STEM) further shows clear differences in the final film morphology after annealing (Fig. 2**g-i**). In the control film, the upper region of the perovskite layer is highly undulated and structurally non-uniform, with pronounced thickness fluctuations and local contrast variations across the film. By contrast, the GuaSCN-treated film exhibits a much flatter and more conformal top region, indicating that, within the analyzed cross-section, the final film surface is structurally more homogeneous after annealing. This distinction is consistent with the GIWAXS results, where the GuaSCN-treated film shows a more directionally correlated scattering pattern, suggesting a more organized near-surface structure.

The compositional ratio maps provide further insight into this difference (Fig. 2**h-j**). In the control film, the Pb/Sn, I/Pb, and I/Sn maps all show substantial spatial fluctuations, particularly in the upper part of the film, indicating that the final perovskite layer is compositionally heterogeneous rather than uniformly mixed. In contrast, the GuaSCN-treated film displays much more homogeneous ratio distributions within the analyzed cross-section, with markedly reduced local fluctuations. This result suggests that GuaSCN suppresses local compositional segregation during film formation and leads to a more uniform final elemental distribution.

Among these maps, the Pb/Sn ratio is particularly informative. The control film contains discrete, localized Pb-rich regions at the upper surface, whereas the GuaSCN-treated film exhibits a much more homogeneous Pb/Sn distribution across its major part, except for a Pb-rich surface region that appears continuous within the analyzed field of view. This implies that the residual secondary structural features detected by GIWAXS are distributed very differently in the two films. In the control film, the non-3D features are more likely associated with local phase segregation or compositionally isolated domains. By contrast, in the GuaSCN-treated film, the more homogeneous Pb/Sn distribution suggests that these residual features are not present as local compositional segregations, but are instead more uniformly integrated into the surrounding perovskite matrix and a Pb-rich surface region that may contribute to surface passivation.

This point is important for interpreting the origin of the weak 2D-related and PbI_2-related diffraction features observed by GIWAXS. From the present data alone, it is difficult to assign the low-dimensional component unambiguously to a specific phase, which may include PbI_2-rich domains, SnI_2-rich domains, or glycine-containing layered phases. However, the combination of GIWAXS and energy-dispersive X-ray spectroscopy (EDS) suggests that, in the GuaSCN-treated film, these residual surface-associated features are more likely distributed in a thin, conformal, and compositionally well-integrated manner, rather than forming discrete and compositionally heterogeneous regions. Therefore, the critical distinction lies not in the presence of secondary phases itself, but in their spatial uniformity and structural compatibility with the surrounding 3D perovskite framework. This more homogeneous surface-near structure in the GuaSCN-treated film is likely beneficial for passivation while preserving the overall compactness of the film.

The improvement in film uniformity is particularly evident at the buried interface. Cross-sectional STEM shows that the control film contains a highly irregular perovskite/substrate contact, with pronounced roughness and local discontinuities near the bottom region. By contrast, the GuaSCN-treated film exhibits a flatter and more continuous buried interface, indicating improved film coalescence. This interpretation is further supported by bottom-view SEM images, which provide a broader-area view of the substrate/perovskite contact (Figure S7). The control film shows an inhomogeneous buried-interface morphology with

apparent voids, whereas the GuaSCN-treated film displays a more continuous and compact buried interface with fewer visible voids. Together with the more homogeneous Pb/Sn, I/Pb, and I/Sn distributions observed by EDS (Fig. 2**j**), these results indicate that GuaSCN suppresses structural and compositional heterogeneity not only near the top surface but also at the buried interface. This improved interfacial continuity is particularly important for HTL-free devices because direct contact between the perovskite and electrode makes device operation highly sensitive to local voids, leakage pathways, and interfacial recombination.

The structural and compositional homogenization induced by GuaSCN can be further correlated with the energetic landscape of the films, as revealed by the spatially resolved quasi-Fermi level splitting (QFLS) maps in Fig. 3**a**. For the glass/PVK configuration, which primarily reflects the intrinsic optoelectronic quality of the perovskite film without contact to the buried ITO interface, the GuaSCN-treated sample

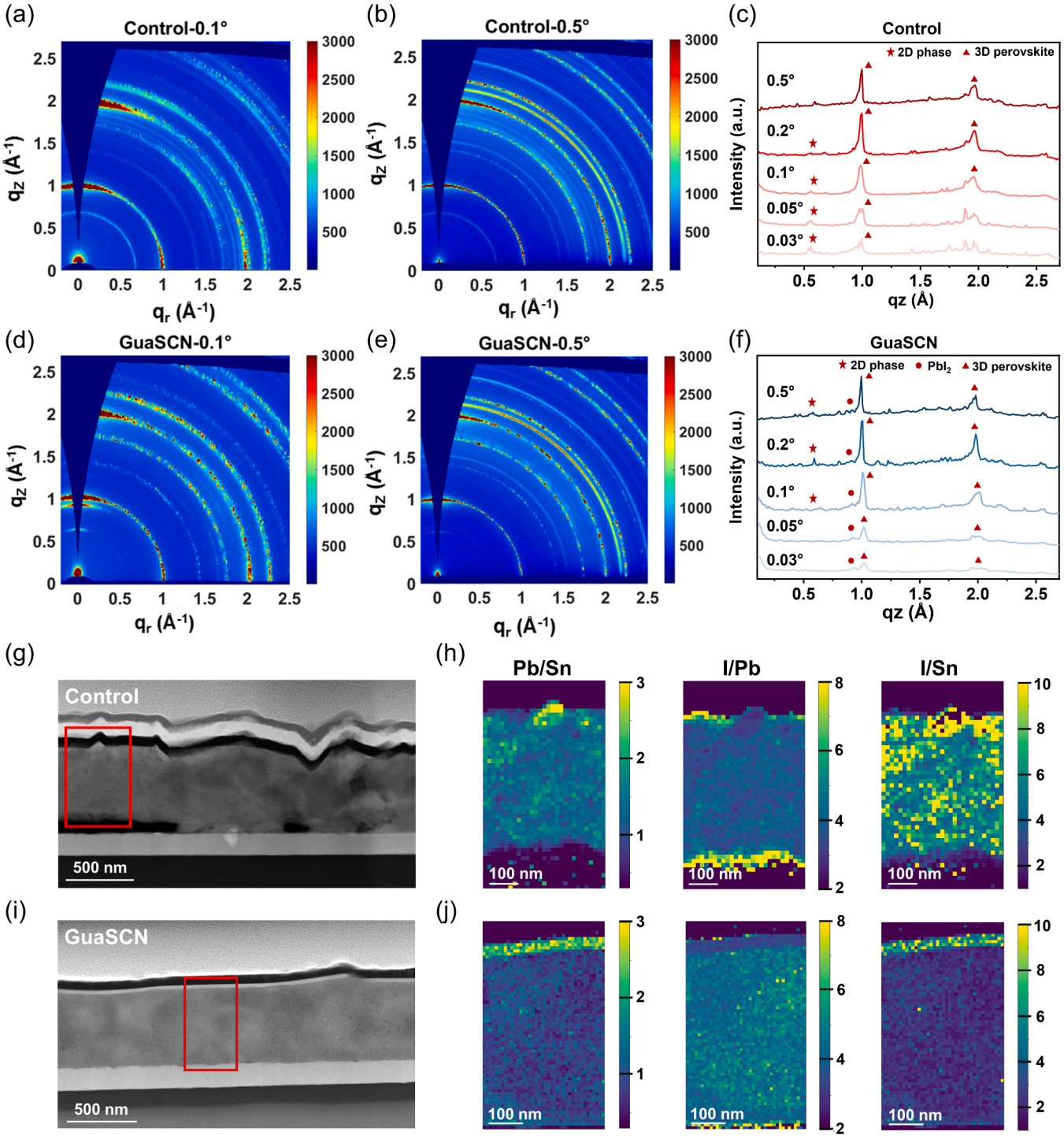

Fig. 2. (a) (b) 2D GIWAXS patterns of the control film measured at incident angles of 0.1° and 0.5°, respectively. (c) Corresponding out-of-plane linecuts of the control film at different incident angles. (d) (e) 2D GIWAXS patterns of the GuaSCN-treated film measured at incident angles of 0.1° and 0.5°, respectively. (f) Corresponding out-of-plane linecuts of the GuaSCN-treated film at different incident angles. (g) (i) Cross-sectional STEM images of the control and GuaSCN-treated films, respectively. (h) (j) STEM-EDS compositional ratio maps of Pb/Sn, I/Pb, and I/Sn extracted from the regions highlighted in (g) and (i), respectively.

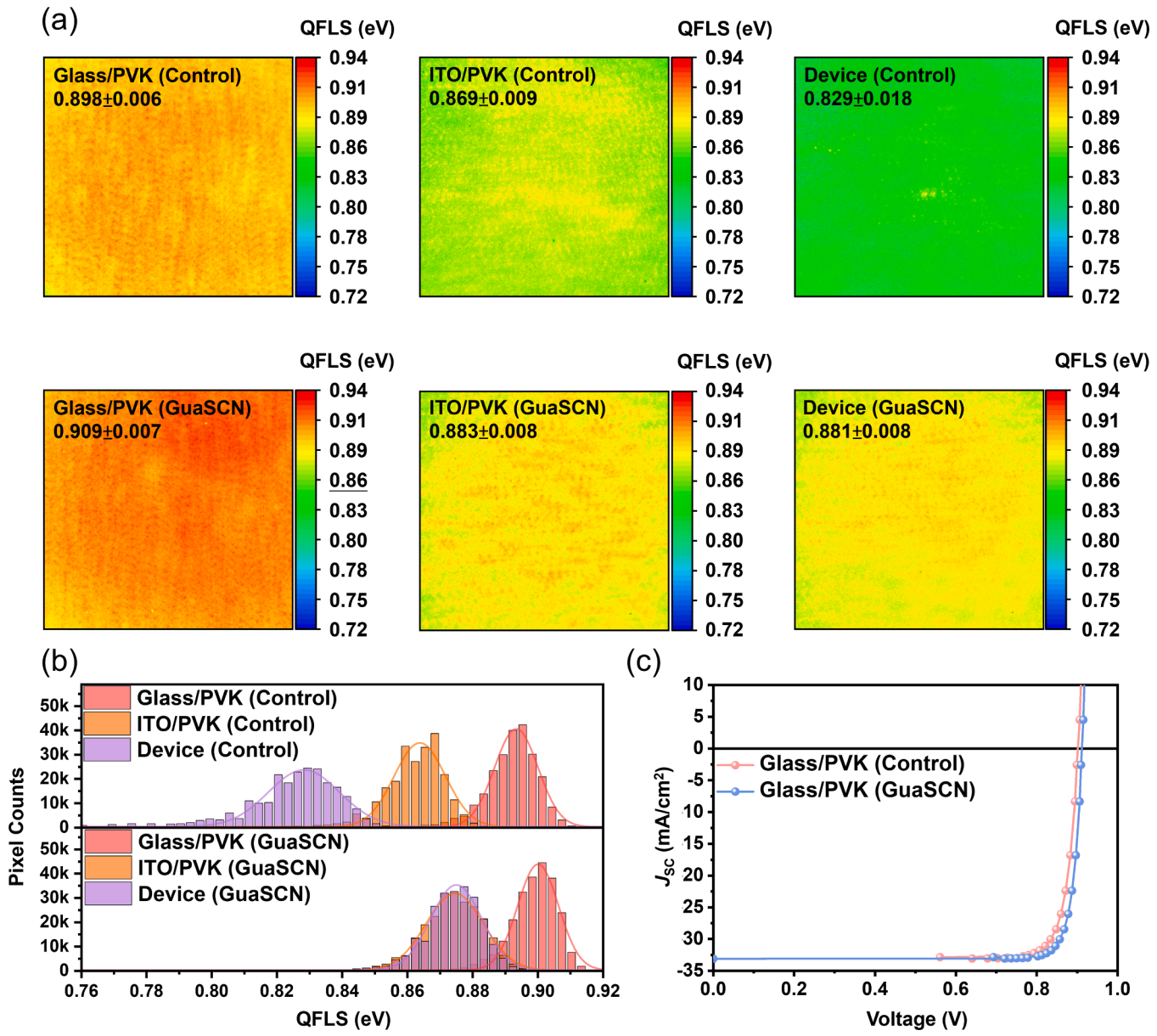

Fig. 3. (a) Spatially resolved QFLS maps of the Glass/PVK, ITO/PVK, and full-device configurations without and with GuaSCN. (b) Corresponding pixel-level QFLS distributions extracted from the QFLS maps. (c) Pseudo *J-V* curves reconstructed from the intensity-dependent QFLS measurements. The histograms represent pixel-based spatial distributions within the mapped areas and are intended to visualize spatial homogeneity rather than independent experimental statistics.

shows a slightly higher and more uniform QFLS distribution than the control, consistent with improved optoelectronic quality at the perovskite level. A more pronounced difference is observed for the ITO/PVK configuration, where the GuaSCN-treated film exhibits both a higher average QFLS and a narrower spatial distribution. This result is consistent with the cross-sectional STEM and compositional mapping (Fig. 2g-j), which showed that GuaSCN substantially reduces structural and compositional heterogeneity at the perovskite/ITO buried interface.

The trend becomes even clearer in the full device stack, where the control sample shows a markedly lower QFLS of approximately 0.83 eV together with broader spatial fluctuation, whereas the GuaSCN-treated device exhibits a higher and more homogeneous QFLS distribution of approximately 0.88 eV, corresponding to an improvement of about 50 meV. Notably, introduction of the top contact produces a pronounced QFLS reduction relative to the ITO/PVK configuration for the control sample, whereas little additional QFLS loss is observed for the GuaSCN-treated sample. This configuration-dependent trend is consistent with reduced recombination losses associated with the top contact after GuaSCN treatment. Together with the surface-associated PbI_2- or 2D-related structural features identified by GIWAXS and STEM, these observations suggest that such residual phases may contribute to reducing recombination at the perovskite/C60 interface, although their specific role cannot be established from the QFLS measurements alone.

To further assess how these energetic improvements translate into the attainable photovoltage in the perovskite thin film, pseudo *J-V* curves were reconstructed from the intensity-dependent QFLS measurements for the glass/PVK configuration (Fig. 3**c**). Because this architecture excludes charge-transport contacts, the resulting pseudo *J-V* reflects the recombination-limited photovoltaic potential of the perovskite film itself. Relative to the control, the GuaSCN-treated film shows a clear right-shift of the pseudo *J-V* curve, with the implied V_{OC} increasing from 0.899 to 0.910 V and the implied PCE improving from 25.64% to 26.56%. The implied fill factor also increases from 86.19% to 88.25%, further supporting the improved energetic quality of the neat perovskite film. Taken together, these results are consistent with improved energetic uniformity, reduced non-radiative recombination losses, and a

higher intrinsic photovoltaic potential after GuaSCN treatment.

To quantitatively relate the internal and external photovoltages, the device-level QFLS/q was compared with the measured V_{OC}, yielding offsets (QFLS/q - V_{OC}) of −25 and + 8 mV for the control and GuaSCN-treated devices, respectively. Since QFLS/q and V_{OC} can differ appreciably when contact selectivity or interfacial transport is imperfect, [50] the near-zero offsets observed here suggest that the measured V_{OC} closely follows the internal QFLS, with limited additional voltage loss arising from contact selectivity or transport. This agreement is particularly noteworthy for the HTL-free architecture, where the absence of a dedicated hole-selective layer might otherwise be expected to compromise contact selectivity. The slightly negative offset of the control likely reflects differences in illumination history and effective timescale between the PL and *J-V* measurements.

Ambient pressure photoemission spectroscopy (APS) further shows changes in the electronic structure at both the buried and top surfaces. APS spectra show clear shift of the valence band edge positions to deeper energies in the samples containing GuaSCN, both at the top and bottom surfaces (Figure S8), indicating that GuaSCN modifies the electronic environment of both surfaces. When considered together with the GIWAXS and STEM-EDS results, these shifts are consistent with surface-associated structural or compositional modifications that may involve 2D-perovskite- or PbI2-rich regions. However, the APS results alone do not directly establish the formation of a passivation layer. The conduction-band edge positions estimated from the optical bandgaps should be interpreted cautiously, since the surface region may contain wider-bandgap phases. Separately, work-function measurements reveal a pronounced front/back asymmetry (Figure S9). The buried side exhibits a much shallower Fermi level than the top side, suggesting the presence of an interfacial dipole layer. We hypothesize that the observed work-function asymmetry may promote band bending at the ITO/perovskite interface and thereby contribute to selective charge transfer in the HTL-free devices, although the interfacial electric field was not directly measured.

The photovoltaic performance of the corresponding HTL-free Sn-Pb perovskite solar cells is shown in Fig. 4**a**. Compared with the control device, the GuaSCN-treated device shows a clear improvement in photovoltaic performance, primarily through increases in V_{OC} and FF, while the J_{SC} shows a moderate increase. The statistical distributions of the photovoltaic parameters reveal improved reproducibility of the GuaSCN-treated devices, with narrower distributions in PCE, V_{OC}, fill factor, and J_{SC} compared with the control devices (Figure S10 and Table 1). Consistently, the integrated current densities derived from the

Table 1
Summary of photovoltaic parameters for control and GuaSCN-treated HTL-free Sn-Pb perovskite solar cells.

	PCE (%)	V_{OC} (V)	FF (%)	J_{SC} (mA/cm^2)	Cal. J_{SC} (mA/cm^2)
Control	16.2 ± 1.3 (17.4)	0.833 ± 0.017 (0.854)	72.4 ± 4.1 (71.4)	28.38 ± 1.40 (28.75)	29.8
GuaSCN	20.9 ± 0.7 (21.4)	0.861 ± 0.006 (0.873)	77.4 ± 1.6 (80.8)	30.82 ± 0.79 (30.67)	30.9

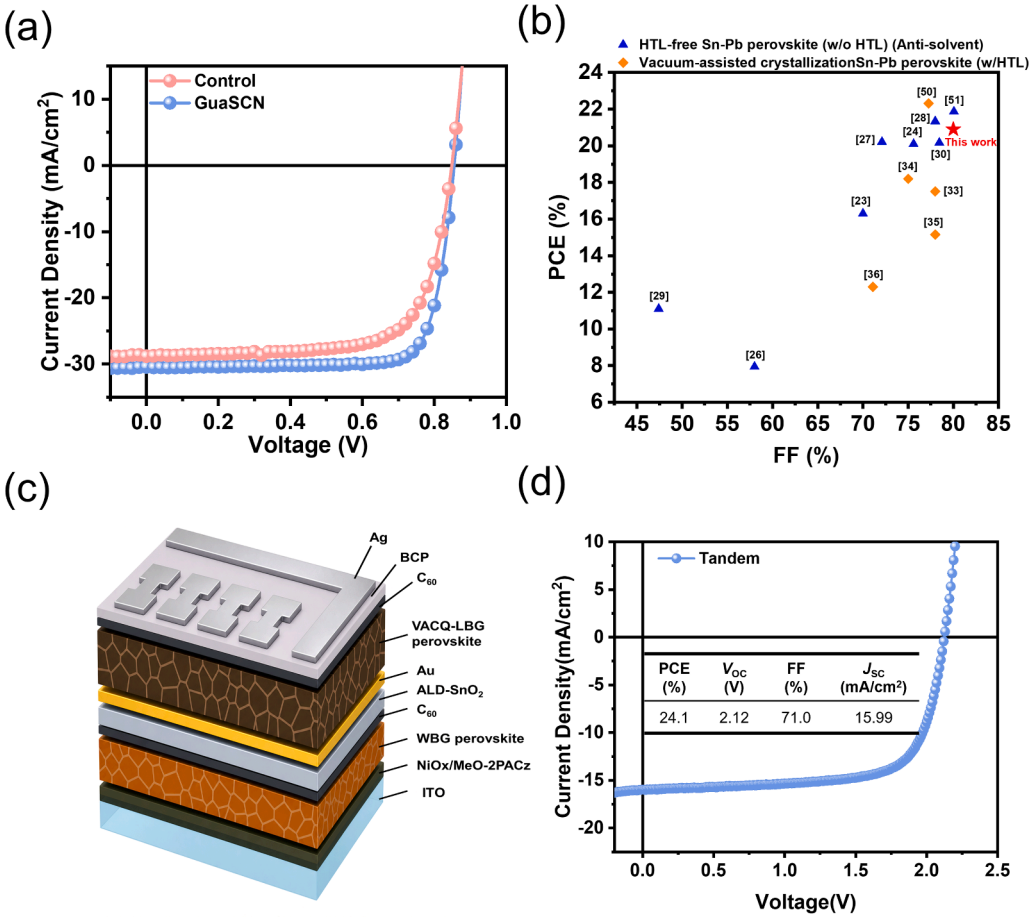

Fig. 4. (a) *J-V* curves of the champion HTL-free Sn-Pb perovskite solar cells without and with GuaSCN. (b) Comparison of the present device with previously reported Sn-Pb perovskite solar cells in a PCE-FF plot. [51] (c) Schematic illustration of the monolithic all-perovskite tandem device using the GuaSCN-treated narrow-bandgap subcell. (d) *J-V* curve of the corresponding champion tandem device.

external quantum efficiency (EQE) spectra agree well with the *J-V* measurements, confirming the reliability of the measured photocurrent (Figure S11). This device performance is consistent with the improved crystallization control, interfacial uniformity, and energetic homogeneity discussed above.

As a result, the GuaSCN-treated HTL-free device delivers a champion power conversion efficiency of 21.4% with a fill factor exceeding 80%, placing it among the highest-performing HTL-free, antisolvent-free Sn-Pb perovskite solar cells reported so far. The simultaneous improvement in *Voc* and FF is particularly significant for HTL-free architectures, where the absence of a hole-transport layer generally makes device operation much more sensitive to buried-interface quality, interfacial leakage, and non-radiative losses. To further understand the origin of the improved photovoltaic parameters, recombination and charge-transport analyses were performed on the complete devices. The GuaSCN-treated device exhibits a substantially lower dark current density than the control device, indicating suppressed leakage pathways and reduced shunt-related losses in the HTL-free architecture (Figure S12). Transient photovoltage measurements show a longer carrier lifetime for the GuaSCN-treated device, consistent with reduced recombination, while transient photocurrent measurements indicate faster charge extraction dynamics (Figure S13). Capacitance analysis and light-intensity-dependent photovoltage measurements also reveal modified interfacial charge distribution and improved photovoltage behaviour after GuaSCN incorporation (Figure S14). In addition, charge extraction measurements show a shorter extraction time and higher carrier mobility for the GuaSCN-treated device, further supporting more efficient charge transport and collection (Figure S15). These device-level results directly support the structural and energetic analyses above, indicating that the GuaSCN-assisted VACQ process effectively mitigates the leakage, recombination, and extraction losses typically associated with simplified HTL-free device configurations. Moreover, a detailed comparison with conventional antisolvent-treated films is provided in the Supporting Information (Figures S16 and S17), further confirming the importance of VACQ as a suitable crystallization platform for HTL-free Sn-Pb perovskite solar cells.

To further place the present result in context, the device performance landscape in Fig. 4**b** compares our HTL-free Sn-Pb perovskite solar cell with previously reported literature devices using a PCE-FF plot, based on the performance data summarized in Table S3. Notably, the present device occupies the upper-right region of the distribution, highlighting a highly competitive combination of both efficiency and fill factor. This is especially important because fill factor is often one of the most difficult parameters to maintain in HTL-free Sn-Pb perovskite solar cells. More importantly, our device achieves this level of performance under an HTL-free and anti-solvent-free configuration, which further underscores the strength of the present strategy. While many previous high-performing Sn-Pb devices rely on sophisticated hole-transport layers and carefully optimized antisolvent processing, the combined use of GuaSCN additive engineering and vacuum-assisted crystallization quenching here enables similarly competitive performance in a much simpler device architecture.

The improved interfacial and energetic quality also translates into enhanced device stability. During storage ageing under conditions consistent with an ISOS-D-1I-style protocol, the GuaSCN-treated devices retain a substantially higher fraction of their initial PCE than the control devices, demonstrating improved storage stability after GuaSCN-treated VACQ processing (Figure S18). The GuaSCN-treated devices also exhibit improved operational stability under conditions consistent with an ISOS-L-1-style protocol. Paraffin-encapsulated devices were continuously illuminated under one-sun conditions in ambient air at approximately 25 °C and 30% relative humidity while operated under an MPP load. After 350 min, the GuaSCN-treated devices retained approximately 94% of their initial PCE, compared with approximately 80% for the control devices (Figure S19 **and** Table S4). In addition, the stabilized photovoltaic output was evaluated by holding the devices at their maximum-power-point voltage under continuous one-sun illumination in a nitrogen-filled glovebox (Figure S20). These results consistently indicate enhanced device stability following GuaSCN-treated VACQ processing, in agreement with the reduced buried-interface voids, suppressed leakage pathways, and lower interfacial recombination losses discussed above.

Finally, to demonstrate the compatibility of the GuaSCN-treated narrow-bandgap Sn-Pb perovskite subcell with tandem-relevant architectures, a proof-of-concept monolithic all-perovskite tandem device was fabricated. The tandem device architecture is shown in Fig. 4**c**, in which the HTL-free GuaSCN-treated Sn-Pb perovskite serves as the narrow-bandgap subcell and the corresponding *J-V* curve is presented in Fig. 4**d**. The tandem device delivers a PCE of 24.1%, with a V_{OC} of 2.12 V, an FF of 71.0%, and a J_{SC} of 15.99 mA cm^{-2}. Although further optimization of the tandem stack is beyond the scope of this work, this result demonstrates the feasibility of incorporating an HTL-free low-bandgap subcell into a monolithic all-perovskite tandem device, underscoring the potential of the GuaSCN-treated VACQ strategy for simplified tandem photovoltaics. Taken together, these results highlight the merit of integrating compositional engineering with process control to simultaneously improve morphology, interfacial quality, energetic uniformity, device performance, and stability.

3. Conclusion

In summary, we developed a GuaSCN-assisted vacuum crystallization strategy for efficient HTL-free and antisolvent-free Sn-Pb perovskite solar cells. Comparative analysis of the GuaI-, $Pb(SCN)_2$-, and GuaSCN-containing formulations shows a characteristic thermal PL evolution that is consistent with complementary effects arising from the combined GuaSCN precursor chemistry. In contrast to previous studies that established the beneficial effects of GuaSCN in antisolvent-processed, HTL-based Sn–Pb devices, the present work connects GuaSCN-assisted VACQ processing with film and buried-interface formation directly on bare ITO and with the mitigation of the associated device losses in an HTL-free architecture. This additive-dependent response enables the favourable optoelectronic evolution observed during thermal annealing after the VACQ process to be translated into compact film formation, more coherent structural organization, homogeneous Pb/Sn distribution, and a flatter, more continuous buried interface. The resulting reduction in structural and compositional heterogeneity leads to improved energetic uniformity, enhanced quasi-Fermi level splitting, and a higher intrinsic photovoltaic potential. As a result, the corresponding HTL-free devices achieve a champion power conversion efficiency of 21.4% with a fill factor exceeding 80%, together with improved reproducibility and storage stability. In addition, a proof-of-concept monolithic all-perovskite tandem device demonstrates the compatibility of the GuaSCN-treated narrow-bandgap subcell with tandem-relevant architectures. More broadly, this work highlights additive-guided crystallization as a powerful strategy for overcoming the interfacial penalties of simplified HTL-free device architectures and supports its potential as a viable processing route for high-performance low-bandgap perovskite subcells in tandem photovoltaics.

CRediT authorship contribution statement

Yun-Shan Li: Writing – review & editing, Writing – original draft, Validation, Data curation. **Wen-Xian Zhu:** Writing – review & editing, Writing – original draft, Validation, Data curation. **Xin Chen:** Writing – original draft, Formal analysis, Data curation. **Yueyao Dong:** Formal analysis, Data curation. **Huan-Wei Lin:** Formal analysis, Data curation. **Yi-Sheng Lin:** Formal analysis, Data curation. **Yun-Sheng Shih:** Formal analysis, Data curation. **Chi-Jing Huang:** Formal analysis, Data curation. **Wei-Jia Qiu:** Formal analysis, Data curation. **Chang-Hao Wang:** Formal analysis. **Chih-Chan Tsai:** Formal analysis. **Luis Lanzetta:** Formal analysis. **Matyas Daboczi:** Formal analysis. **Caterina Ducati:**

Supervision, Formal analysis. **Eric Wei-Guang Diau:** Supervision, Formal analysis. **Thomas J. Macdonald:** Writing – review & editing, Supervision, Formal analysis. **Chieh-Ting Lin:** Writing – review & editing, Writing – original draft, Supervision, Formal analysis, Data curation, Conceptualization.

Declaration of Competing Interest

The authors declare that they have no known competing financial interests or personal relationships that could have appeared to influence the work reported in this paper

Acknowledgements

C.-T. L. thanks to the National Science and Technology Council (114–2628-E-005–001 -, 114–2622-E-005–001 -, 115–2927-I-005–502 -, 115–2628-E-005–001 -, 114–2634-F-005–002 -), and Innovation and Development Center of Sustainable Agriculture from The Featured Areas Research Center Program within the framework of the Higher Education Sprout Project by the Ministry of Education (MOE) in Taiwan. T.J.M. thanks the Royal Commission for the Exhibition of 1851 for their financial support through a Research Fellowship. T.J.M. also acknowledges funding from a Royal Society University Research Fellowship (URF/R1/221834) and the Royal Society Research Fellows Enhanced Research Expenses (RF/ERE/221066). E.W.-G.D gratefully thank Dr. Y.-W. Tsai and Dr. J.-M. Lin (TPS 25A1, NSRRC) for their kind assistance in GIWAXS data analysis. E.W.-G.D also acknowledge the support by the National Science and Technology Council (NSTC), Taiwan (Grant Nos. NSTC 113–2639-M-A49–001-ASP and NSTC 114–2639-M-A49–001-ASP), and the Center for Emergent Functional Matter Science of National Yang-Ming Chiao-Tung University (NYCU) from the Featured Areas Research Center Program within the framework of the Higher Education Sprout Project by the Ministry of Education (MOE) in Taiwan. X.C. and C.D. acknowledge the use of the Thermo Fisher Spectra 300 TEM funded by EPSRC under grant EP/R008779/1. TEM studies were supported by access to Cambridge Wolfson Electron Microscopy Suites (WEMS). Dr Simon Fairclough is acknowledged for his support on training and operation of advanced STEM characterization. L.L. acknowledges support from the European Union's Horizon Europe research and innovation programme under the Marie Skłodowska-Curie Actions Postdoctoral Fellowship (grant agreement No. 101153098).

Appendix A. Supporting information

Supplementary data associated with this article can be found in the online version at doi:10.1016/j.mser.2026.101283.

Data availability

Data will be made available on request.

References

[1] J.Y. Kim, J.W. Lee, H.S. Jung, H. Shin, N.G. Park, Chem. Rev. 120 (2020) 7867.
[2] G. Kapil, T. Bessho, Y. Sanehira, S.R. Sahamir, M. Chen, A.K. Baranwal, D. Liu, Y. Sono, D. Hirotani, D. Nomura, K. Nishimura, M.A. Kamarudin, Q. Shen, H. Segawa, S. Hayase, ACS Energy Lett. 7 (2022) 966.
[3] M. Zhang, D. Chi, J. Wang, F. Wu, S. Huang, Sol. Energy 201 (2020) 589.
[4] J. Werner, T. Moot, T.A. Gossett, I.E. Gould, A.F. Palmstrom, E.J. Wolf, C.C. Boyd, M.F.A.M. Van Hest, J.M. Luther, J.J. Berry, M.D. McGehee, ACS Energy Lett. 5 (2020) 1215.
[5] A. Goyal, S. McKechnie, D. Pashov, W. Tumas, M. Van Schilfgaarde, V. Stevanović, Chem. Mater. 30 (2018) 3920.
[6] H. Hu, S. Moghadamzadeh, R. Azmi, Y. Li, M. Kaiser, J.C. Fischer, Q. Jin, J. Maibach, I.M. Hossain, U.W. Paetzold, B.Abdollahi Nejand, Adv. Funct. Mater. 32 (2022) 2107650.
[7] R. Lin, Y. Wang, Q. Lu, B. Tang, J. Li, H. Gao, Y. Gao, H. Li, C. Ding, J. Wen, P. Wu, C. Liu, S. Zhao, K. Xiao, Z. Liu, C. Ma, Y. Deng, L. Li, F. Fan, H. Tan, Nature 620 (2023) 994.
[8] R. Lin, J. Xu, M. Wei, Y. Wang, Z. Qin, Z. Liu, J. Wu, K. Xiao, B. Chen, S.M. Park, G. Chen, H.R. Atapattu, K.R. Graham, J. Xu, J. Zhu, L. Li, C. Zhang, E.H. Sargent, H. Tan, Nature 603 (2022) 73.
[9] L. Lanzetta, T. Webb, N. Zibouche, X. Liang, D. Ding, G. Min, R.J.E. Westbrook, B. Gaggio, T.J. Macdonald, M.S. Islam, S.A. Haque, Nat. Commun. 12 (2021) 2853.
[10] A. Alsulami, L. Lanzetta, L. Huerta Hernandez, D. Rosas Villalva, A. Sharma, S. P. Gonzalez Lopez, A.H. Emwas, A. Yazmaciyan, F. Laquai, I. Yavuz, D. Baran, J. Am. Chem. Soc. 146 (2024) 22970.
[11] J. Zhou, S. Fu, S. Zhou, L. Huang, C. Wang, H. Guan, D. Pu, H. Cui, C. Wang, T. Wang, W. Meng, G. Fang, W. Ke, Nat. Commun. 15 (2024) 2324.
[12] Z. Zhang, J. Liang, Y. Zheng, X. Wu, J. Wang, Y. Huang, Y. Yang, Z. Zhou, L. Wang, L. Kong, K.M. Reddy, C. Qin, C.C. Chen, J. Mater. Chem. A 9 (2021) 17830.
[13] S.-E. Hsu, W.-X. Zhu, D.-T. Wu, W.-L. Huang, L.-T. Xue, C.-J. Huang, C.-H. Wang, Y.-S. Li, W.-J. Qiu, C.-T. Lin, Sustain. Energy Fuels 8 (2024) 1712.
[14] W. Xu, T. Du, M. Sachs, T.J. Macdonald, G. Min, L. Mohan, K. Stewart, C.-T. Lin, J. Wu, R. Pacalaj, S.A. Haque, M.A. McLachlan, J.R. Durrant, Cell. Rep. Phys. Sci. 3 (2022) 100890.
[15] Y. Dong, F.M. Rombach, G. Min, H.J. Snaith, C.-T. Lin, S.A. Haque, T.J. Macdonald, Materials Science Engineering R Reports 162 (2025) 100875.
[16] S. Lee, M.Y. Woo, C. Kim, K.W. Kim, H. Lee, S.B. Kang, J.M. Im, M.J. Jeong, Y. Hong, J.W. Yoon, S.Y. Kim, K. Heo, K. Zhu, J.S. Park, J.H. Noh, D.H. Kim, Chem. Eng. J. 479 (2024) 147587.
[17] D.-T. Wu, W.-X. Zhu, Y. Dong, M. Daboczi, G. Ham, H.-J. Hsieh, C.-J. Huang, W. Xu, C. Henderson, J.-S. Kim, S. Eslava, H. Cha, T.J. Macdonald, C.-T. Lin, Small Methods 8 (2024) 2400302.
[18] Q. Wang, C.C. Chueh, M. Eslamian, A.K.Y. Jen, ACS Appl. Mater. Interfaces 8 (2016) 32068.
[19] P. Guo, J. Dong, C. Xu, Y. Yao, J. You, H. Bian, W. Zeng, G. Zhou, X. He, M. Wang, X. Zhou, M. Wang, Q. Song, J. Mater. Chem. A 11 (2023) 7246.
[20] Z.Y. Huang, W.J. Qiu, C.H. Wang, Y. Dong, M. Daboczi, Y.C. Shih, P.H. Chiu, Y. S. Li, C.J. Huang, C.W. Ko, S. Eslava, C.S. Huang, T.J. Macdonald, C.T. Lin, Mater. Today Energy 53 (2025) 101979.
[21] Q. Han, Y. Wei, R. Lin, Z. Fang, K. Xiao, X. Luo, S. Gu, J. Zhu, L. Ding, H. Tan, Sci. Bull. (Beijing) 64 (2019) 1399.
[22] Y. Sun, Y. Lai, Y. Yang, Small 6 (2024) 2406991.
[23] J. You, H. Bian, M. Wang, X. Cai, C. Li, G. Zhou, H. Lu, C. Fang, J. Huang, Y. Yao, C. Xu, Q. Song, J. Energy Chem. 85 (2023).
[24] T. Ma, H. Wang, Z. Wu, Y. Zhao, C. Chen, X. Yin, L. Hu, F. Yao, Q. Lin, S. Wang, D. Zhao, X. Li, C. Wang, Adv. Mater. 36 (2024) 2308240.
[25] H. Liu, J. Sun, H. Hu, Y. Li, B. Hu, B. Xu, W.C.H. Choy, ACS Appl. Mater. Interfaces 13 (2021) 45059.
[26] H. Kim, J.W. Lee, G.R. Han, Y.J. Kim, S.H. Kim, S.K. Kim, S.K. Kwak, J.H. Oh, Adv. Funct. Mater. 32 (2022) 2110069.
[27] S. Moghadamzadeh, I.M. Hossain, M. Loy, D.B. Ritzer, H. Hu, D. Hauschild, A. Mertens, J.P. Becker, A.A. Haghighirad, E. Ahlswede, L. Weinhardt, U. Lemmer, B.A. Nejand, U.W. Paetzold, ACS Appl. Mater. Interfaces 13 (2021) 46488.
[28] Y. Liao, X. Jiang, W. Zhou, Z. Shi, B. Li, Q. Mi, Z. Ning, Front. Optoelectron. 10 (2017) 103.
[29] X. Chang, J.X. Zhong, G. Yang, Y. Tan, L. Gong, X. Ni, Y. Ji, Y. Li, G. Zhang, Y. Zheng, Y. Shao, J. Zhou, Z. Yang, L. Wang, W.Q. Wu, Sci. Bull. (Beijing) 68 (2023) 1271.
[30] G. Liu, G. Yang, W. Feng, H. Li, M. Yang, Y. Zhong, X. Jiang, W.Q. Wu, Adv. Mater. 36 (2024) 2405860.
[31] H. Sun, K. Deng, J. Xiong, L. Li, Adv. Energy Mater. 10 (2020) 1903347.
[32] J. Zhang, H. Hu, Y. Zhang, Z. Liang, P. Zhu, Z. Li, D. Wang, J. Chen, J. Zeng, Z. Jiang, J. Wu, L. Zhang, B. Hu, X. Pan, X. Wang, B. Xu, ACS Appl. Mater. Interfaces 15 (2023) 15321.
[33] Z. Zhang, Y. Huang, C. Wang, Y. Jiang, J. Jin, J. Xu, Z. Li, Z. Su, Q. Zhou, J. Zhu, R. He, D. Hou, H. Lai, S. Ren, C. Chen, X. Gao, T. Shi, W. Hu, F. Fu, P. Gao, D. Zhao, Energy Environ. Sci. 16 (2023) 3430.
[34] S. Ghosh, S. Mishra, T. Singh, Adv. Mater. Interfaces 7 (2020) 2000950.
[35] C. Li, Y. Pan, J. Hu, S. Qiu, C. Zhang, Y. Yang, S. Chen, X. Liu, C.J. Brabec, M. K. Nazeeruddin, Y. Mai, F. Guo, ACS Energy Lett. 5 (2020) 1386.
[36] B. Abdollahi Nejand, I.M. Hossain, M. Jakoby, S. Moghadamzadeh, T. Abzieher, S. Gharibzadeh, J.A. Schwenzer, P. Nazari, F. Schackmar, D. Hauschild, L. Weinhardt, U. Lemmer, B.S. Richards, I.A. Howard, U.W. Paetzold, Adv. Energy Mater. 10 (2020) 1902583.
[37] L. Zeng, Z. Chen, S. Qiu, J. Hu, C. Li, X. Liu, G. Liang, C.J. Brabec, Y. Mai, F. Guo, Nano Energy 66 (2019) 104099.
[38] M. Liu, Z. Chen, Q. Xue, S.H. Cheung, S.K. So, H.L. Yip, Y. Cao, J. Mater. Chem. A 6 (2018) 16347.
[39] J. Tong, Z. Song, D. Hoe Kim, X. Chen, C. Chen, A.F. Palmstrom, P.F. Ndione, M. O. Reese, S.P. Dunfield, O.G. Reid, J. Liu, F. Zhang, S.P. Harvey, Z. Li, S. T. Christensen, G. Teeter, D. Zhao, M.M. Al-Jassim, M.F.A.M. van Hest, M.C. Beard, S.E. Shaheen, J.J. Berry, Y. Yan, K. Zhu, Science (1979) (364) (2019) 475.
[40] Y. Dong, W.X. Zhu, D.T. Wu, X. Li, R.J.E. Westbrook, C.J. Huang, Z. Min, W. Hong, B. Wang, G. Min, S. Sathasivam, M. Palma, S. Dimitrov, C.T. Lin, T.J. Macdonald, J. Am. Chem. Soc. 147 (2025) 31578.
[41] A.D. Jodlowski, C. Roldán-Carmona, G. Grancini, M. Salado, M. Ralaiarisoa, S. Ahmad, N. Koch, L. Camacho, G. De Miguel, M.K. Nazeeruddin, Nat. Energy 2 (2017) 972.
[42] S. Hu, P. Zhao, K. Nakano, R.D.J. Oliver, J. Pascual, J.A. Smith, T. Yamada, M. A. Truong, R. Murdey, N. Shioya, T. Hasegawa, M. Ehara, M.B. Johnston, K. Tajima, Y. Kanemitsu, H.J. Snaith, A. Wakamiya, Adv. Mater. 35 (2023) 2208320.

[43] J.A. Steele, E. Solano, D. Hardy, D. Dayton, D. Ladd, K. White, P. Chen, J. Hou, H. Huang, R.A. Saha, L. Wang, F. Gao, J. Hofkens, M.B.J. Roeffaers, D. Chernyshov, M.F. Toney, Adv. Energy Mater. 13 (2023) 2300760.
[44] H. Zheng, G. Liu, Y. Wang, F. Chen, X. Dong, C. Wang, C. Wu, L. Yang, X. Ren, L. Yang, X. Pan, Z. Huang, Adv. Funct. Mater. 34 (2024) 2401546.
[45] C.-T. Lin, W. Xu, T.J. Macdonald, J. Ngiam, J.-H. Kim, T. Du, S. Xu, P.S. Tuladhar, H. Kang, K. Lee, J.R. Durrant, M.A. McLachlan, ACS Appl. Mater. Interfaces 13 (2021) 43505.
[46] H. Zheng, W. Wu, H. Xu, F. Zheng, G. Liu, X. Pan, Q. Chen, Adv. Funct. Mater. 30 (2020) 2000034.
[47] C.-T. Lin, J. Lee, J. Kim, T.J. Macdonald, J. Ngiam, B. Xu, M. Daboczi, W. Xu, S. Pont, B. Park, H. Kang, J.-S. Kim, D.J. Payne, K. Lee, J.R. Durrant, M. A. McLachlan, Adv. Funct. Mater. 30 (2020) 1906763.
[48] Y. Zhang, L. Xu, Y. Wu, H. Zhang, F. Zeng, J. Xing, B. Liu, Y. Qi, B. Dong, X. Bai, H. Song, Adv. Funct. Mater. 33 (2023) 2214102.
[49] J. Warby, S. Shah, J. Thiesbrummel, E. Gutierrez-Partida, H. Lai, B. Alebachew, M. Grischek, F. Yang, F. Lang, S. Albrecht, F. Fu, D. Neher, M. Stolterfoht, Adv. Energy Mater. 13 (2023) 2303135.
[50] C. Ge, Q. Xu, D. Liu, W. Ye, Y. Zhu, P. Zhang, J. Yang, G. Liang, L. Xu, Y. Zhou, H. Song, C. Chen, J. Tang, Energy Environ. Sci. 18 (2024) 430–438.
[51] Y. Xu, J. You, J. Zhu, Y. Xu, J. Jin, P. Jiang, Q. Gao, Z. Gao, J. Wang, W. Jiao, Y. Luo, T. Ma, K. Wu, S. Ren, C. Chen, C. Wang, D. Zhao, ACS Appl. Mater. Interfaces 17 (2025) 28300.

Chieh-Ting Lin Chieh-Ting Lin is an Associate Professor in the Department of Chemical Engineering at National Chung Hsing University, Taiwan. He received his Ph.D. in Materials Science from Imperial College London in 2020 under the supervision of Prof. James R. Durrant and Prof. Martyn McLachlan. Following his doctoral studies, he conducted postdoctoral research at Imperial College London and Gwangju Institute of Science and Technology (GIST), South Korea. His research focuses on perovskite optoelectronic devices, including tin–lead perovskite solar cells, HTL-free device architectures, photodetectors, and photoelectrochemical systems. His current interests include interfacial engineering, charge-carrier dynamics, and ion migration in perovskite semiconductors.

Thomas J. Macdonald Thomas J. Macdonald is an Associate Professor and University Research Fellow in the Department of Electronic & Electrical Engineering at University College London. He previously held a prestigious 1851 Research Fellowship at Imperial College London. Before this, he was a Ramsay Memorial Fellow in the Department of Chemistry at University College London working on nanomaterials for solar energy conversion. He obtained his Ph.D. at the University of South Australia in 2016 working in the research group of Prof. Thomas Nann. He has a strong interest in renewable energy and extensive experience in the synthesis of functional nanomaterials and the fabrication of third-generation photovoltaics.